

A phase averaged PIV study of circular and non-circular synthetic turbulent jets issuing from sharp edge orifices

A. Hashiehba^f, G.P. Romano^{*}

Department of Mechanical and Aerospace Engineering, La Sapienza University, Via Eudossiana n18, 00184 Rome, Italy

ARTICLE INFO

Keywords:

Mixing enhancement
Axis switching
Synthetic jet
Non-circular jet
Sharp edge orifice
PIV

ABSTRACT

An extensive experimental study using Particle Image Velocimetry (PIV) on synthetic jets issuing from different orifice shapes is reported. All data are phase and time averaged to derive mean velocity, half-velocity width and *rms* velocity profiles in the near field of the jet ($0 < X/D < 7$), at a Reynolds number around 10,000. Different non-circular orifice shapes as rectangular, square, elliptic and triangular are considered and results are compared to those of the circular orifice in order to investigate the effect of asymmetry on the turbulent flow field in view of mixing enhancement. The measurements are carried out on two orthogonal planes to capture three dimensional features of non-circular jets. Results show highest velocity decay rate for elongated orifices, especially the rectangular one, in comparison to the circular one, both in phase and time-averaged plots. Time averaged results show higher velocity decay rate of synthetic jets in comparison to those of continuous ones. It is also observed that, for $X/D > 5$, only profiles of circular and square jets become partially self-similar. For synthetic jets, higher turbulence content is measured for all orifice shapes at the centerline and close to the orifice exit in comparison to continuous jets.

1. Introduction

Synthetic jets are those jets generated without any steady flow in the background, *i.e.*, the average mean velocity during one blowing-suction cycle is zero, even if momentum flux is different from zero (Mohseni and Mittal, 2014). This is due to the fact that there are always vortices escaping from the orifice in the ejection phase which would not be totally drawn back during successive suction, thus generating a net momentum flux. In other words, there are non-equal positive and negative peak velocities in the ejection and suction phase, respectively. Specifically, the maximum velocity in the ejection phase always occurs at the centreline of the turbulent jet, whereas it occurs far from the centreline of the jet (nearly at the edges of the orifice) in the suction phase (Shuster and Smith, 2007). There are different mechanisms for producing such jet such as piston-cylinder alternation (Gilarranz et al., 2005), oscillating membrane (Mossi et al., 2005) and acoustic excitation (Tesar and Kordik, 2009). The use of above described mechanisms, allows achieving many important engineering applications of such non-circular synthetic jets, as those in cooling of electronic devices or turbine blades, drag reduction over aerofoils, underwater vehicle propulsion and pulsatile injectors in combustors (Lee et al., 2016; Amitay et al., 2001; Mangate et al., 2019).

One of the fundamental investigations in the area of synthetic jets is

the work by Cater and Soria (2002). They investigated a pulsating jet for large Reynolds numbers ($Re = 10,000$) and small Strouhal numbers (*e.g.*, 0.0015), by increasing the amplitude of oscillation in a piston mechanism. Their main result is that the Reynolds number, based on a velocity scale of the blowing cycle, and the Strouhal number are indeed the two dominant parameters in determining the jet structure. In these conditions, the self-similar behavior in the mean velocity profiles is reached at a distance from the outlet equal to $X/D = 15$ (where D is the jet equivalent diameter), which is higher than that obtained more recently by other authors as Di Cicca and Iuso (2007) *i.e.*, $X/D = 6$, and Chaudhari et al. (2009), $X/D = 7$. In any case, these distances are smaller than those measured in continuous jets. Di Cicca and Iuso (2007) correlated the earlier self-similarity of axial velocity in synthetic jets, in comparison to continuous ones, to the earlier development of mixing layer instabilities and so far to the local increased mixing. At small Reynolds numbers ($Re = 1732$) and relatively high Strouhal number ($St = 0.041$), a series of vortex rings with little entrainment of ambient fluid was observed, as in Watson et al. (2003), so that the self-similarity region is delayed, coming closer to that of continuous jets. Trying to summarize all possible patterns, Glezer (1988) proposed a vortex map for laminar, transitional and turbulent conditions, by analysing the developing vortex rings in the ejection phase. This was further investigated also by Shuster and Smith (2007) who studied the

^{*} Corresponding author.

E-mail address: giampaolo.romano@uniroma1.it (G.P. Romano).

Nomenclature

D	equivalent circular orifice inlet diameter (m)	U_o	mean exit velocity during ejection phase (m/s)
H	orifice width (m)	u_{rms}	mean Stream-wise <i>rms</i> velocity (m/s)
K	cycle duty factor	v_{rms}	mean Cross-wise <i>rms</i> velocity (m/s)
L	stroke length (m)	w_{rms}	mean Span-wise <i>rms</i> velocity (m/s)
Re	Reynolds number ($Re = U_{ex}D/\nu$)	X	stream-wise coordinate (m)
St	Strouhal number ($St = U_{ex} t/D$)	X_s	saddle back point
T	cycle period (s)	Y	lateral coordinate (m)
U	mean exit velocity along orifice width (m/s)	$y_{0.5}(m)$	half-velocity width in y direction (m)
U_{cl}	velocity at centerline of the jet (m/s)	Z	cross-wise coordinate (m)
U_{ex}	peak exit velocity during ejection phase (m/s)	$z_{0.5}$	half-velocity width in z direction (m)
		ν	dynamic viscosity of the fluid (m^2/s)

effect of Reynolds number and stroke length in an extensive range ($Re = 1000\text{--}10,000$, $L/D = 1\text{--}3$). They observed “trailing jet” formation at stroke lengths $4 < L/D < 5$, as also proposed by Gharib et al. (1998), while no vortex ring was observed for $L/D < 0.6$.

Regarding the shape of the orifice, Watson et al. (2003) performed qualitative measurements on the effect of such a parameter on vortex structure formed in the near field of a pulsatile jet, observing that even with the same velocity peak value at the exit plane of each orifice, the developed vortex rings from rectangular jets were completely turbulent while being laminar for the circular one. Smith and Glezer (2007) extended the investigation to plane synthetic jets, in a nearly laminar flow regime, due to a quite large Strouhal number ($St > 0.03$), according to criterion reported in Cater and Soria (2002). In agreement with previously reported measurements, they found that the fully developed self-similar axial velocity was achieved much closer to the orifice exit ($X/H > 10$), in respect to continuous plane jets ($X/H > 40$). They showed that time averaged cross-wise profiles of axial velocity and turbulent fluctuations, for both synthetic and continuous jets, are similar to each other, the only difference being related to the decrease of centreline velocity as $x^{-0.58}$, in comparison to the decay $x^{-0.5}$ of continuous jets. O’Farrell and Dabiri (2013) investigated the vortex ring formation on elliptic orifices with aspect ratio, AR, equal to 2 and 4 and also oval orifice. They extended the definition of formation number

previously introduced by Gharib et al. (1998) for non-circular vortex rings.

Also Lio et al. (2007) investigated the effects of different orifice shapes, showing that vortices formed on the minor axis of elongated orifices move towards the jet axis and grow faster in respect to those at the major one, which move away from the jet. This leads to the well-known axis switching phenomenon, observed in non-circular continuous jets (Hashiehbaf and Romano, 2013). As a consequence, vortex rings formed in circular orifice move faster downstream in respect to those from rectangular ones. Wang et al. (2018) investigated the effect of orifice shape with different aspect ratio on mixing enhancement in the near field of the jet ($X/D < 10$). They reported occurrence of two axis switching for both rectangular and elliptic orifices for $AR = 3$, but only one for $AR = 5$. Shi et al. (2019) investigated circular and elliptic synthetic jets with different aspect ratio in the laminar regime, concluding that low aspect ratio elliptic nozzles have higher entrainment rate in respect to circular ones and reported that increases of stroke length results in decreasing of the number of axis switching. Wang et al. (2010) investigated the effect of duty cycle factor K ($K = T_2/T_1$, where T_2 is the suction stroke period and T_1 is the ejection stroke period) on pulsed planar orifice jets with aspect ratio $AR = 100$. They showed that the vortex formed at the orifice moves faster downstream for high values of K in respect to smaller ones, whereas the distance between

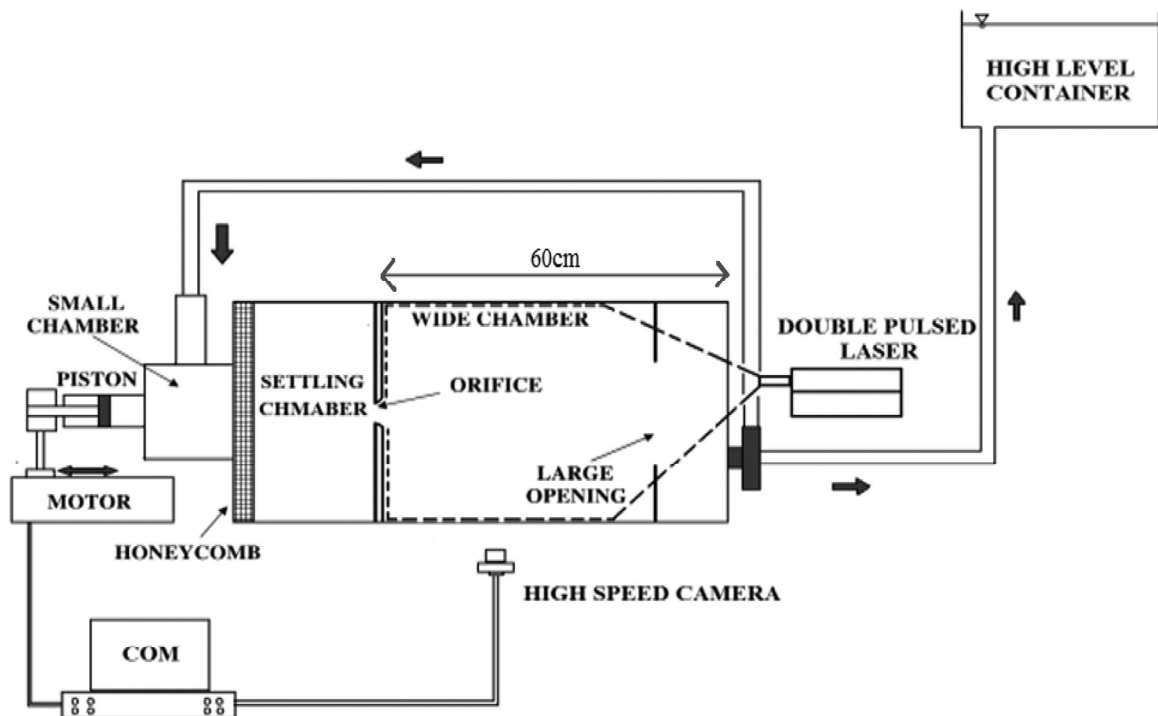


Fig. 1. Schematic view of the experimental setup with flow from left to right from the orifice.

vortex pairs is much larger for higher K in comparison to smaller ones. The resulting effect is a higher spreading rate in comparison to the continuous and mixed pulsed jets (Mossi et al., 2005; Tesar and Kordik, 2009).

Regarding mean square velocity fluctuations, Di Cicca and Iuso (2007) noted a reduction of turbulence by increasing the frequency for a fixed stroke length, in agreement with findings of Pratomo and Bremhorst (2006). Frequency and amplitude of forcing oscillations also contribute to this effect, as observed by Qayoum et al. (2010), the higher being the frequency, the lower the fluctuating velocity.

The observation of results obtained in literature for continuous jets, suggests that the shape of orifice could have a dominant effect on the developing mean and fluctuating velocity fields, in addition to the dependence on stroke length and Reynolds number (Falchi et al., 2010). Moving from here, the aim of this paper is to investigate differences among vortex generation and development in pulsed jets, downstream orifices of different shape in fully turbulent conditions, which are extremely interesting for engineering application. The attention is focused onto mean and fluctuating velocity fields, by looking at phase and time averaged results in view of possible mixing enhancements. Specifically, the results obtained on velocity decay and self-similarity will be

Table 1

Orifice characteristic size.

Orifice type	Major axis(mm)	Minor axis(mm)	Area (mm^2)
Circular	20.0	20.0	100π
Rectangular	10.2	30.7	100π
Elliptic	11.5	34.7	100π
Triangular	23.3	13.5	100π
Square	17.7	17.7	100π

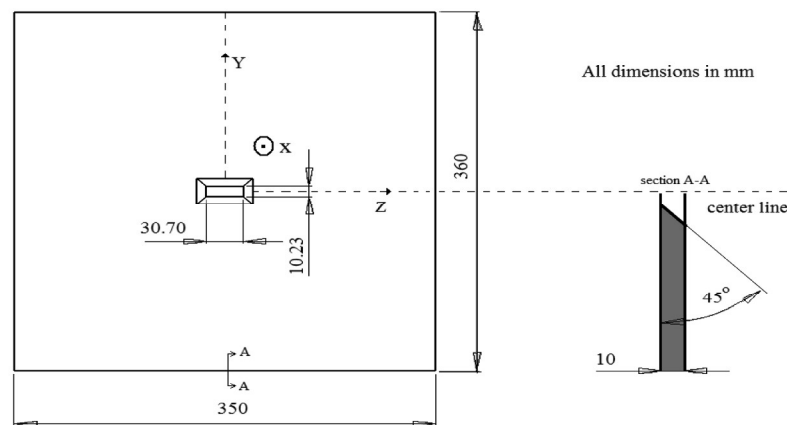
compared among the different orifice shapes and among pulsating and continuous conditions.

2. Experimental facility, measurement technique and data analysis

A sketch of the experimental setup and real images of high quality (sharp edge, roundness less than 0.5 mm) manufactured non-circular orifices are shown in Figs. 1 and 2. Five different orifice shapes are cut through a plate as orifice jets, the geometrical configurations employed in present experiments being circular, rectangular, squared, elliptical and triangular. The plate dimensions on the measurement planes (X-Y &



a)



b)

Fig. 2. Real images of orifice orifices (a) and detailed dimension of the rectangular orifice and wide chamber (b).

X-Z) are also depicted in Fig. 2b for the rectangular orifice as an example.

As a matter of fact, in an orifice jet it is not possible to consider fully developed flow, so it is not possible to use hydraulic diameter concept. Therefore, the orifice inlet area is fixed for all configurations as equal to the inlet area of circular orifice used for comparison ($D = 2$ cm), the details being given in Table 1.

Due to reciprocating motion of the piston, driven by a linear motor, the water flows into the wide chamber (test section) from the small chamber, through the same sharp edge orifices and the same facility used for continuous jets (Hashiehbaf and Romano, 2013). Finally, the water flows out from a large, circular, opening (20 cm in diameter) made on a Plexiglas plate. Both the water inlet and outlet were connected to a constant-head container through two one-way valves. Theoretically, these valves should cancel the backflow through the orifice during the backward motion of the piston, so far allow keeping the same inlet conditions at each pulse. In practice, this will not be exactly the case as reported at the beginning of Section 3. The linear motor driving the piston is controlled by LABVIEW software on a PC, allowing different specific velocity programs to be fed to the piston.

Both vertical and horizontal mid-planes of the wide chamber are illuminated separately by a Nd-YAG laser (covering X-Y & X-Z plane) in double pulse mode. The number of laser pulses is synchronized to the period of piston velocity program, which results in 20 pulses at 10 Hz for each cycle. The light sheet thickness is approximately 2 mm. The water was seeded with hollow glass particles (8–10 μ m diameter), allowing to follow the fluid flow oscillations up to 10^5 Hz (Stokes frequency). A high speed CMOS camera is mounted perpendicular to the light sheet, working at full resolution (1024×1024 pixel) and capturing 500 frames/s, by following a trigger signal synchronised with the motion of the piston (therefore the time interval between double PIV images in 2 ms). The region of interest is divided into two $8 \text{ cm} \times 8 \text{ cm}$ window size (with an overlapping of 2 cm between two windows), covering seven and four equivalent diameters from the orifice exit in streamwise and vertical directions, respectively. The whole cycle period is divided into 20 phases, each producing the minimum time resolution of 0.1 s (considering that the frequency of the piston is 0.5 Hz). To ensure statistical convergence, five different acquisitions, each containing 2000 images, are carried out in each window. The phase averaging method is employed here for averaging the instantaneous velocity fields acquired in each phase of the cycle. Thus, for each phase, 500 images are available for each phase averaging (10,000 total images/20 phases), which have been proved to be large enough for convergence of first and second-order statistics (variations less than $\pm 5\%$ for the average after 50 cycles and after 200 cycles for the *rms* velocity).

Mean velocity, streamwise and lateral *rms* velocity fields are obtained using a PIV image analysis software (LaVision GmbH), with final interrogation window of 32×32 pixels with 75% overlap which results in a grid data of 128×128 vectors. Therefore, the distance between two data points is 0.625 mm. The piston displacement is feedback controlled by a PC, therefore, if there is any difference between the input signal and the output displacement larger than 0.2 mm, the piston motion is modified accordingly. Hence, since the average piston stroke length is around 13.7 cm, the maximum error regarding the piston position is approximately 0.14%. Basically, this is also the relative error on the timing of the piston, thus the possible lag in phase averaging procedures (being timing error on laser emission much smaller than this). A sinusoidal input velocity program with a time period of $T = 2$ s is selected for producing the pulsation in the flow, whereas the amplitude of oscillation is related to the stroke volumes ejected through the orifice (90 mL). Each input signal for the piston is given in the form of 200 data points, allowing to reach a Reynolds number equal to 10,000 based on the peak exit velocity ($Re_{U_{ex}}$) and 2000 based on the average velocity (Re_{U_0}), with a Strouhal number equal to 0.022.

Phase averaged statistics is evaluated by using the triple decomposition method proposed by Hussain and Reynolds (1970) and by Reynolds averaging over the total number of images captured at each time interval (phase)

$$u_n(x, t) = u'_n(x, t) + \bar{u}_n(x) + \tilde{u}_n(x, t) \quad (5-1)$$

where u_n is the n^{th} instantaneous velocity component, \bar{u}_n is the time-averaged velocity component, \tilde{u}_n is the phase-correlated velocity component and u'_n is the turbulent fluctuation. They are defined as following

$$\bar{u}_n(x) = \lim_{T \rightarrow \infty} \frac{1}{T} \int_0^T u_n(x, t) dt \quad (5-2)$$

$$\langle u_n(x, t) \rangle = \lim_{N \rightarrow \infty} \frac{1}{N} \sum_{n=0}^N u_n(x, t + \alpha\tau) \quad (5-3)$$

$$u'_n(x, t) = u_n(x, t) - \langle u_n(x, t) \rangle \quad (5-4)$$

$$\tilde{u}_n(x, t) = \langle u_n(x, t) \rangle - \bar{u}_n(x) \quad (5-5)$$

where $\langle u_n(x, t) \rangle$ is the phase-averaged velocity component, N is the number of the instantaneous velocity fields at the same phase, α is an integer and τ is the period of the coherent contribution, which in this study is considered as the period of forcing generating the synthetic jet.

By knowing the total number of 40 images acquired in each cycle (based on the laser pulse rate and pulse number in each second), it is possible to consider that the first and second image are correlated in time similarly to the (1 + 40)th & (2 + 40)th in the second cycle, the (1 + 80)th & (2 + 80)th in the third cycle and so on. Thus all of them belong to the first phase ($t/T = 0.1$) and averaging over all image pairs will give the phase average at this specific phase. The same procedure would be repeated for the 3rd and 4th images and also (3 + 40)th & (4 + 40)th, (3 + 80)th & (4 + 80)th, ... to produce the images pairs for averaging in the second phase ($t/T = 0.2$) and so on until all time intervals of the cycle are considered. The mean ejection velocity is computed from integration of velocity profile in ejection phase as the velocity scale for normalization, based on the definition of Glezer (1988).

$$U_0 = \frac{\int_0^T u(t) dt}{T} \quad (5-6)$$

where $u(t)$ is the exit velocity profile and T is period of oscillation.

Due to the complex nature of the phenomenon, an uncertainty analysis based on the approach of Sciacchitano (2016) is performed for all orifice types at two selected phase instants, for more comprehensive understandings the results being presented in Tables 2 and 3.

3. Results and discussion

The axial velocity is evaluated for each of the 20 phases, by averaging the local instantaneous exit velocity (as close as possible to the orifice exit, $X/D \approx 0.1$) along the orifice width and normalizing it by

Table 2

Estimated values of error on mean and *rms* velocities at jet centerline for reverse flow ($t = 0.7T$).

Orifice shape	Mean velocity (U)	Fluctuating velocity U_{rms}	Fluctuating velocity V_{rms}
	Centerline mean error	Centerline mean error	Centerline mean error
Circular	5.51%	7.93%	4.48%
Square	6.1%	7.67%	4.27%
Triangular	3.38%	9%	4.41%
Elliptic	6.04%	8.12%	6.58%
Rectangular	4.95%	8.44%	4.97%

Table 3

Estimated values of error on mean and *rms* velocities at jet centerline around peak ejection ($t = 0.4T$).

Orifice shape	Mean velocity (U)	Fluctuating velocity U_{rms}	Fluctuating velocity V_{rms}
	Centerline mean error	Centerline mean error	Centerline mean error
Circular	1.68%	4.1%	4.64%
Square	1.46%	5%	4.15%
Triangular	1.37%	7.92%	4.91%
Elliptic	2.06%	4.4%	4.17%
Rectangular	2.4%	5%	4.7%

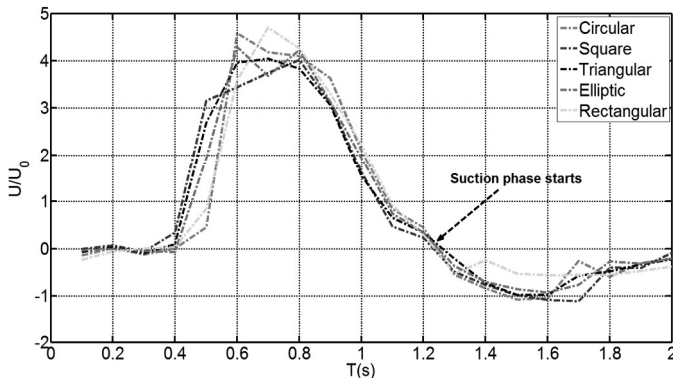


Fig. 3. Normalized averaged axial velocity at the exit of the orifice for different orifices.

Table 4

Estimated values of volumetric efficiency for the different jets.

Orifice	Average exit velocity (m/s)	ε
Circular	0.10	0.78
Square	0.10	0.75
Triangular	0.11	0.79
Elliptic	0.10	0.80
Rectangular	0.11	0.82

the time averaged exit velocity. Values are plotted in Fig. 3 for the different orifice shapes over the whole time period, also as a check of inlet conditions for the different jets. The behavior of all jets is quite similar, except possibly for the rectangular orifice, which is showing some delay and change especially during the backward motion of the piston, *i.e.*, the suction phase. This could be related to the different vortex evolution mechanism across the different orifices, which will be detailed in the following. Peak ejection velocity is around four times larger than the suction velocity, in agreement with results of Jain et al. (2011). As stated in Section 2, the whole fluid volume pumped by the piston is passing through the orifices whatever their shape, but curves in Fig. 3 are non-symmetrical during injection and suction phases, due to the closure of the valve during the latter. Specifically, the fluid exhibits an unwanted small backflow into the settling chamber due to the deformation of the wide chamber and to imperfections in the hydraulic circuit. During suction, the maximum backward velocity occurs at the edge of orifices as will be shown in the following. Actually, this also indicates that the present jets are no longer ZNMF (or pure synthetic jets), the present condition being more strictly considered as related to hybrid synthetic jets (Tesar et al., 2006; Trávníček et al., 2006). So far, it is important to characterize the amount of deviation from a pure synthetic jet and if this amount would be almost the same for all orifices. This can be quantified by using the volumetric efficiency ε , *i.e.*, the ratio of the net output fluid volume to the total displaced volume pumped during the oscillation period. This quantity is derived for the

present jet configurations, from spatial profiles at the inlet section and at the different phases (being an integral quantity, it is not so much affected by poor resolution in phase) and is presented in Table 4. The results show that the value of volumetric efficiency changes from a minimum $\varepsilon \approx 0.75$ for the square geometry to a maximum $\varepsilon \approx 0.82$ for the rectangular one, giving a maximum difference around 9%. Therefore, considering the rather small amount of this difference, it is possible to state that the present jets are forming at the same inlet and boundary conditions and that eventually the small differences are affecting the unwanted backflow (which is not considered in detail in this paper).

3.1. Phase averaged data

Based on relation (5–6), the normalized phase averaged axial velocity contour maps for different orifices under investigation are shown in Fig. 4 for $t/T = 0.3, 0.35, 0.4, 0.45$ and 0.75 in each figure. Ejected vortices can be observed in all orifice types, with the highest velocity being measured for circular orifice ($U/U_0 = 6.175$) and triangular orifice ($U/U_0 = 5.831$). Despite, by looking at the circular orifice at $t/T = 0.45$ (Fig. 4a), it is evident that a second vortex, separated from the leading one, exists in the flow field. This is related to the observation made by Gharib et al. (1998) of a limiting maximum circulation and vorticity in the growth of an isolated vortex, the circulation in excess being responsible for the generation of other vortices. This phenomenon is only partially observed for square and triangular orifices, with a kind of merging among two separated vortex cores (Fig. 4b and c). For elongated orifices (rectangular and elliptic), separated maxima of axial velocity are not observed behind the leading vortex and this could be due to the severe axis switching observed in these type of jets (Fig. 4d, e and f). The axis switching phenomenon could be recognized by looking at major axis evolution of rectangular orifice shown in Fig. 4f at $t/T = 0.35$ – 0.4 .

At the beginning of the suction phase ($t/T = 0.75$), close to the orifice exit, negative values can be seen for all configurations in the form of dark blue regions on the left hand side of Fig. 4. Indeed, the position where the negative velocity values change sign is named saddle back and is evaluated from Fig. 4 and labeled as X_s in each plot. This position is slightly dependent on the orifice type and for all occurs at X/D less than unity, the rectangular orifice showing the shortest saddle back point distance from the orifice exit (less than 0.9).

To identify in higher detail phase averaged vortices, vorticity maps are reported in Fig. 5 at $t/T = 0.3, 0.35, 0.4$ and 0.45 . In each map, three phase averaged plots are overlapped: absolute normalized value of vorticity (color lines, scale on the right), velocity vectors and axial velocity color maps normalized by average velocity in ejection phase (color background, scale on the left). Accordingly to Fig. 5a, for the circular jet, the absolute value of velocity is decreasing by 25% from $t/T = 0.3$ to $t/T = 0.45$ and vorticity also decreases for first vortex from $t/T = 0.3$ to $t/T = 0.4$. The generation of the second vortex is clearly observed in this sequence, as also the strongly reduced amount of vorticity associated in comparison to the leading vortex.

The second vortex is generated at $t/T = 0.4$ – 0.45 , in agreement with first vortex pinch off from the trailing jet, starting from $t/T = 0.3$ and completed at $t/T = 0.45$. As already pointed out in the comments to Fig. 4, this secondary vortex ring has been observed in impulsive starting circular jets (Gharib et al., 1998) and in the present experiments could be retained as a consequence of an ambient fluid almost at rest before starting a new ejection phase at each cycle. The pinch off phenomenon is not observed for any of the other jet configurations, so that this exemplifies a completely different vortex structure in circular orifice, which is also the reason for high turbulence fluctuations at the centerline, as described later. For the square jet, reported in Fig. 5b, the overall content of velocity and vorticity is lower in respect to the circular one, however basically showing similar trailing jet behavior, except for the lack of any pinch off. A second very weak vortex appears